

LiDAR, GNSS and IMU Sensor Alignment through Dynamic Time Warping to Construct 3D City Maps

Haitian Wang^a, Hezam Albaqami^{b,*}, Xinyu Wang^a, Muhammad Ibrahim^a,
Zainy M. Malakan^c, Abdullah M. Algamdi^b, Mohammed H. Alghamdi^{d,e},
Ajmal Mian^a

^a*Department of Computer Science and Software Engineering, University of Western Australia, 35 Stirling Highway, Crawley, Perth, 6009, Western Australia, Australia*

^b*Department of Computer Science and Artificial Intelligence, College of Computer Science and Engineering, University of Jeddah, Jeddah, 21493, Saudi Arabia*

^c*Data Science Department, Umm Al-Qura University, Makkah, 24382, Saudi Arabia*

^d*Department of Information and Technology Systems, College of Computer Science and Engineering, University of Jeddah, Jeddah, 21493, Saudi Arabia*

^e*Department of Informatics and Computer Systems, College of Computer Science, King Khaild University, Abha, Saudi Arabia*

Abstract

LiDAR-based 3D mapping suffers from cumulative drift causing global misalignment, particularly in GNSS-constrained environments. To address this, we propose a unified framework that fuses LiDAR, GNSS, and IMU data for high-resolution city-scale mapping. The method performs velocity-based temporal alignment using Dynamic Time Warping and refines GNSS and IMU signals via extended Kalman filtering. Local maps are built using Normal Distributions Transform-based registration and pose graph optimization with loop closure detection, while global consistency is enforced using GNSS-constrained anchors followed by fine registration of overlapping segments. We also introduce a large-scale multimodal dataset captured in Perth, Western Australia to facilitate future research in this direction. Our dataset comprises 144,000 frames acquired with a 128-channel Ouster LiDAR, synchronized RTK-GNSS trajectories, and MEMS-IMU measurements across 21 urban loops. To assess geometric consistency, we evaluated our method using alignment metrics based on road centerlines and intersections to capture both global and local accuracy. Our method reduces the average global

*Corresponding author: haalbaqamii@uj.edu.sa

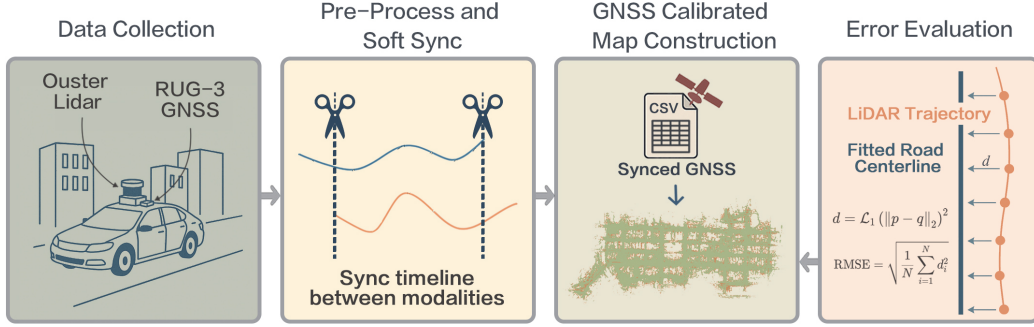


Figure 1: Overview of the proposed framework for 3D city mapping which comprises: (1) multimodal data capture via Ouster OS1-128 LiDAR and RUG-3 GNSS/IMU; (2) preprocessing with velocity-based alignment and Dynamic Time Warping synchronization; (3) GNSS-calibrated 3D mapping using NDT, pose graph optimization, and global ICP; and (4) accuracy evaluation via skeleton-based centreline metrics against 2D cartographic references.

alignment error from 3.32 m to 1.24 m, achieving a 61.4% improvement. The constructed high-fidelity map supports a wide range of applications, including smart city planning, geospatial data integration, infrastructure monitoring, and GPS-free navigation. Our method, and dataset together establish a new benchmark for evaluating 3D city mapping in GNSS-constrained environments. The dataset and code will be released publicly.

Keywords: Light Detection & Ranging (LiDAR), Point Cloud, Global Navigation Satellite System, Inertial Measurement Unit, 3D City Mapping

1. Introduction

Urbanization is rapidly transforming cities into dense and complex environments, increasing the demand for scalable infrastructure planning and maintenance [1, 2]. In this context, updated high-resolution spatial data is essential [3, 4, 5]. However, passive vision-based methods such as photogrammetry [6], stereo vision [7], and Structure-from-Motion (SfM) [8] often struggle in poor or changing lighting conditions, making them unsuitable for detailed city-scale 3D mapping.

Light Detection and Ranging (LiDAR) sensor provides dense 3D data with rich geometric features that are robust to lighting and weather conditions, making it ideal for mapping complex urban environments [9]. LiDAR can accurately capture features such as curbs, intersections, poles, road markings, traffic signs, building facades, sidewalks, overpasses, and street furniture. These capabilities make it a key enabler of precise city-scale 3D mapping. Recent advances, including the integration of solid-state LiDAR and

IMUs [10], fusion with high-precision GNSS [11, 12], and digital LiDAR architectures such as Ouster multibeam sensors [13] have contributed to the advancement of 3D city mapping in dense urban environments [14, 15, 16].

Despite these advancements, LiDAR-based mapping still faces challenges such as cumulative drift during frame-by-frame alignment [17, 18], especially over long trajectories. Although methods like In2Laama [19] address motion distortion through LiDAR-IMU optimization, they lack GNSS integration and do not scale well for large urban deployments. GNSS can help mitigate drift, but in dense cityscape, signals are often degraded or lost due to occlusions by tall buildings, bridges, or tunnels. Moreover, many LiDAR platforms do not include native GNSS receivers, and external units require precise calibration and synchronization. These limitations lead to misalignments that compromise the global consistency and reliability of the final map.

These sensor-level limitations are further compounded by gaps in existing urban mapping datasets. Widely used benchmarks such as KITTI [20, 21, 22], Perth-WA [23] and nuScenes [24] lack reliable GNSS ground truth and globally consistent 3D map alignment. This makes them unsuitable for evaluating city-scale mapping in environments where GNSS signals are degraded. Moreover, datasets such as Toronto-3D [25] and the Melbourne Urban Dataset [26], offer improved spatial coverage but still suffer from sparse road-level detail, frequent occlusions, and reduced accuracy in dense areas. To address some of these challenges, various multi-sensor fusion frameworks [27, 28, 29] and semantic-aided stabilization methods [30, 31, 32] have been developed. However, most are limited to short-ranges and fail to correct cumulative drift or achieve accurate synchronization across modalities in large-scale, GNSS-constrained settings. Furthermore, robust temporal synchronization across heterogeneous sensors remains largely unexplored in existing datasets and methods.

To overcome the challenges of cumulative drift and cross-sensor synchronization in city-scale mapping, we propose LIGMA (LiDAR-IMU-GNSS Mapping Architecture), a unified multimodal fusion framework that integrates data from the three sensors for globally consistent 3D reconstruction. The core novelty lies in a Dynamic Time Warping (DTW)-based velocity matching strategy that enables robust temporal alignment across sensors with varying sampling rates and unsynchronized clocks. To our knowledge, this is the first use of DTW-based synchronization in urban LiDAR-GNSS mapping. Our method further employs a hierarchical registration approach that includes local alignment via Normal Distributions Transform (NDT),

pose graph optimization with loop closure detection, and global refinement using Iterative Closest Point (ICP). GNSS and IMU measurements serve as spatial anchors, mitigating cumulated drift to improve global consistency.

Alongside the proposed framework, we present a high-resolution multisensor dataset collected in the Perth Central Business District (CBD), Western Australia. The dataset comprises 144,000 LiDAR frames from a 128-channel Ouster sensor, accompanied by synchronized RTK-GNSS and IMU measurements across 21 road loops, covering approximately the 4.2, km² region. LiDAR data are preprocessed through Statistical Outlier Removal (SOR) for denoising and voxel grid filtering for downsampling. GNSS and IMU streams are processed with an Extended Kalman Filter and temporally aligned via DTW to ensure consistency across modalities. This dataset provides dense 3D geometry with precise georeferencing and supports benchmarking of city mapping in GNSS-denied or obstructed environments.

We evaluate our method using centreline and intersection-based metrics by comparing the reconstructed 3D maps against high-resolution 2D cartographic references [33, 34]. The proposed method achieves a 61.4% reduction in global alignment error, lowering the RMSE from 3.32m to 1.24m. The modular architecture of the pipeline enables generalization to different sensor configurations and urban layouts, supporting its applicability to broader city-scale mapping scenarios. To promote reproducibility and foster further research, we release our code and dataset.

This work offers the following key contributions:

1. LIGMA framework: A unified sensor fusion pipeline that integrates LiDAR, GNSS, and inertial data using a novel velocity-based alignment and multi-stage registration strategy guided by GNSS/IMU priors.
2. Urban-scale dataset: A high-resolution dataset covering 4.2 km² of central Perth, comprising 144,000 LiDAR frames with synchronized and georeferenced inertial and positioning data.

2. Related Work

Precise and globally consistent 3D urban mapping is essential for applications such as infrastructure monitoring, and city-scale planning [35]. Prior work in LiDAR-based mapping has demonstrated reliable geometric accuracy and robustness to lighting conditions, with methods such as GICP [10] and SLIM framework [36, 37] improving global consistency and scalability. Pose graph optimization [38] and semantic-aware registration, including LCDNet [39] and semantic NDT [40], have addressed drift and

sparse-feature challenges. However, LiDAR-only approaches like LOAM [41], SliceTransformer [42] and LeGO-LOAM [43] remain limited in feature-scarce or high-speed scenarios due to restricted sensing range and insufficient feature extraction capabilities [44]. This degrades the global map accuracy and continuity, especially when using solid-state LiDARs with limited sensor coverage. Additionally, Dynamic Channel-wise Outlier Removal methods have been adopted to de-noise LiDAR data, enabling the construction of more accurate and consistent point cloud maps [28, 45].

To overcome single-sensor limitations, recent studies increasingly adopt multimodal fusion strategies that combine LiDAR, inertial and positioning sensors for enhanced localization and mapping [30, 17, 29]. IMU integration has been shown to reduce drift to a greater extent compared to LiDAR-only baselines such as NDT or ICP [28]. EKF and factor graph methods are foundational to multi-sensor integration, with the latter providing improved scalability in complex urban environments [30]. Synchronization across heterogeneous sensors has also advanced through velocity-based Dynamic Time Warping, aligning LiDAR-derived velocities with IMU profiles to improve temporal coherence [45, 46]. Despite these advances, many synchronization techniques rely on simplistic interpolation or fixed-rate assumptions, which degrade under real-world jitter and asynchronous sampling [47, 48].

Traditional metrics for 3D map evaluation, including absolute pose error, drift per unit distance, and translation error, remain widely used for assessing global alignment. Translation error quantifies deviations from reference centerlines [49, 33], while drift is typically reported per 100 meters, particularly relevant for loop-free mapping scenarios. Map completion rate has also emerged as a robustness metric, especially in non-revisiting trajectories, with methods like SLIM [10] achieving over 90% accuracy. However, these metrics have critical limitations: they depend on costly ground truth from terrestrial laser scanners, and often fail to accurately capture local geometric structures in dynamic or GNSS-constrained environments [50, 45].

These limitations underscore the need for a unified framework that addresses drift and sensor misalignment challenges in city-scale mapping. Our work introduces such a solution, combining multimodal fusion with a benchmark dataset to real-world constraints.

3. Data Collection

This section outlines the data acquisition framework, covering survey objectives, sensor setup, deployment strategy, data formats, and quality assur-

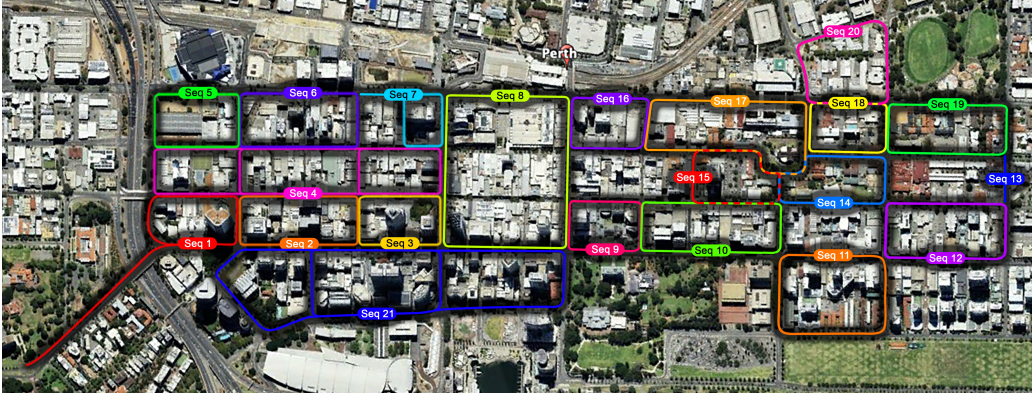


Figure 2: Survey layout of the Perth CBD dataset with 21 manually designed loops (Seq 1–21) spanning 18.6km of urban roads, providing diverse viewpoints, repeated coverage, and intersection overlap for robust SLAM and high-quality 3D mapping.

ance. The goal is to ensure high geospatial accuracy, temporal consistency, and broad urban coverage. The resulting dataset supports downstream tasks including multi-sensor 3D mapping, localization, and change detection.

3.1. Survey Objectives and Study Area Definition

This survey aims to construct a high-precision, multi-sensor 3D point cloud dataset of Perth CBD to support urban mapping, planning, and large-scale monitoring. It also provides a foundation for developing and evaluating algorithms for LiDAR-based SLAM, GNSS–LiDAR fusion, and change detection. Perth CBD was selected for its structural complexity, frequent GNSS occlusions, dynamic traffic, and variable weather—conditions that pose significant challenges for localization, perception, and long-term mapping.

The dataset captures a wide range of urban features, including high-rise buildings, multi-lane roads, laneways, sidewalks, intersections, pedestrian zones, green corridors, and public infrastructure such as signage, transit stops, and light poles. To ensure spatial coverage and temporal redundancy, data collection was structured into 21 manually designed loops totaling 18.6 km, with an average loop length of 931 m. Frequent intersections among loops facilitate loop closure detection and improve spatial consistency. The routes span major and minor roads, one-way streets, and complex junctions, ensuring diverse scene capture from multiple perspectives. As shown in Fig. 2, the survey layout enables repeated traversals and varied viewpoints for robust SLAM and map refinement. Data were collected over several days using a vehicle traveling at 10–30 km/h during low-traffic periods to ensure

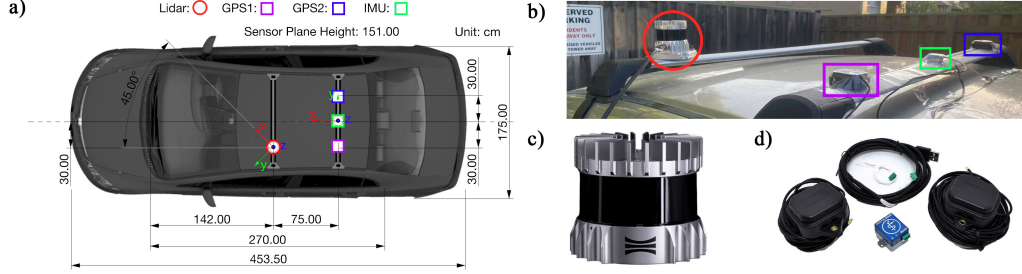


Figure 3: Sensor setup for vehicle-based data collection in central Perth, featuring a roof-mounted 128-channel LiDAR (red), dual GNSS antennas (purple and blue), and a high-grade inertial unit (green), all precisely aligned. (a) Schematic with dimensions, (b) real-world deployment, and (c–d) core sensor modules.

high point density and minimize motion distortion and occlusion.

3.2. Sensor Specifications

The sensing system comprises a 128-channel Ouster OS1 LiDAR and a RUG-3-IMX-5-Dual GNSS-IMU module [51]. The OS1 is a dual-return high-resolution scanner with a 45° vertical field of view, 0.35° angular resolution at 10 Hz, and a peak output of 2.6 million points per second. Each point includes 3D coordinates, intensity, and a time stamp, which supports detailed reconstruction of urban environments [52, 53]. The GNSS-IMU module integrates dual multi-frequency RTK receivers and a high-performance MEMS inertial unit, delivering sub-meter accuracy and full 6-DoF orientation. It supports GPS, GLONASS, Galileo, and BeiDou constellations. According to the manufacturer specifications, the GNSS operates at 5 Hz and the IMU at 73 Hz [54]. Unlike tightly coupled systems, the LiDAR and GNSS-IMU modules operate asynchronously, with synchronization and logging handled by a central acquisition system as detailed in subsection 3.3.

3.3. Sensor Setup and Hardware Configuration

The sensor suite was mounted on a standard passenger vehicle with careful attention to spatial alignment and mechanical stability. As shown in Fig. 3, the setup includes an Ouster LiDAR, dual GNSS antennas, and a GNSS-IMU module, all co-located and geometrically referenced on the roof. The LiDAR was positioned at the front centerline, 1.51 m above ground, offering a clear 360° horizontal field of view. GNSS antennas were rigidly mounted at the front-left and rear-right corners, forming a 1.42 m baseline for yaw estimation. The IMU was placed centrally between the antennas along the vehicle’s longitudinal axis to minimize lever-arm effects and rotational distortion. Temporal synchronization was achieved via a PPS signal

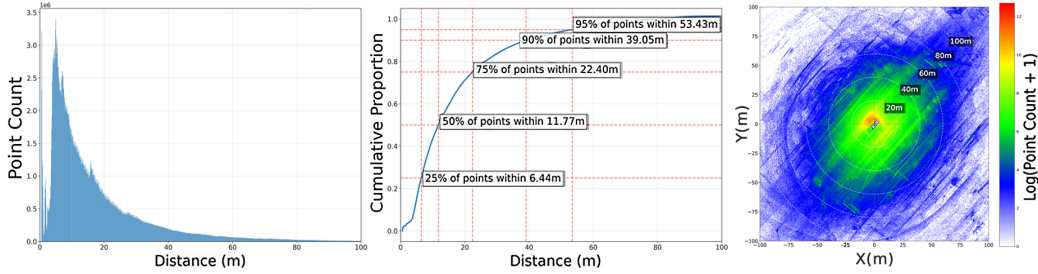


Figure 4: Point cloud distribution and density - Left: Point count histogram vs. distance from LiDAR origin; Middle: Cumulative distribution showing 75% of points within 22.4m; Right: Top-down heatmap with log-scaled point density, highlighting near-field concentration.

from the GNSS receiver, ensuring alignment across sensor streams. Data were logged using manufacturer SDKs: Ouster Sensor SDK for LiDAR and Inertial Sense uINS SDK for GNSS-IMU data. Both sensor modules operate independently and connect to a ruggedized Ubuntu 20.04 laptop: the LiDAR via Gigabit Ethernet and the GNSS-IMU through USB. All data streams are timestamped in real-time using the host clock. The devices were powered by an automotive source 12 V and connected through industrial-grade USB and serial interfaces. Sensor extrinsics were calibrated using manufacturer specifications and verified through constrained-motion routines. All components were housed in weather-resistant enclosures with shielded cable routing to mitigate EMI and vibration.

3.4. Data Modalities, Formats, and Organization

The dataset is organized in a loop-based directory structure (e.g., `/seq01/`, `/seq02/`), with each sequence containing subfolders for LiDAR, GNSS, IMU, calibration, and logs. LiDAR frames were recorded at 10 Hz in dual-return mode using the Ouster OS1-128, producing approximately 380 GB of raw data. Each frame contains 260k–280k points with 3D coordinates, intensity, and ring index, initially saved in `.pcap` format and later converted to `.bin` and `.ply` for downstream use. GNSS and IMU data were logged using the Inertial Sense uINS SDK at 5 Hz and 73 Hz, respectively, and stored in `.csv` format with synchronized Unix timestamps and metadata (e.g., RTK status, satellite visibility). All sensor streams are time-aligned using PPS synchronization and spatially registered via a rigid-body extrinsic matrix defined in `transforms.yaml`. To support benchmarking, the dataset also includes pose graphs, KITTI-format trajectories, and loop closure ground truth. As shown in Fig. 4, point density analysis indicates that 75% of LiDAR returns lie within 22.4m, emphasizing the importance of high-fidelity short-range sensing for urban mapping.

3.5. Quality Assurance and Handling of Imperfections

A multi-stage quality assurance pipeline was implemented to ensure data reliability for SLAM, sensor fusion, and urban perception tasks. During collection, real-time diagnostics monitored LiDAR return rates, satellite visibility (SV count), IMU status, and RTK fix quality via onboard dashboards. Sequences with degraded signals (e.g., SV count < 6 or RTK loss) were flagged for review. Data were captured over multiple low-traffic days to minimize dynamic occlusions. Post-processing included statistical and radius-based filtering to clean LiDAR noise and sparsity, while frames with excessive dropout ($>25\%$) were annotated for exclusion. GNSS trajectories were smoothed using an extended Kalman filter to correct jump artifacts. Temporal alignment was verified by comparing LiDAR odometry with GNSS-IMU dead reckoning, with sequences exceeding 0.5 m residual or 200 ms lag corrected or removed. Calibration was validated through rigid-body residuals and loop closure consistency; loops with drift over 0.3 m were reprocessed or discarded. All quality flags and exclusion masks are stored in YAML metadata for selective processing and robustness evaluation.

4. Methods

This section presents the LIGMA framework for high-precision 3D urban mapping. It leverages tightly coupled integration of LiDAR, GNSS, and IMU data. As shown in Fig. 5, the proposed method comprises four main stages: (1) multimodal preprocessing, including noise filtering, voxel downsampling, interpolation, and state estimation via an Extended Kalman Filter; (2) temporal alignment of LiDAR and IMU streams using velocity-based matching and Dynamic Time Warping; (3) hierarchical mapping through NDT registration, GNSS-constrained loop closure, and ICP refinement; and (4) quantitative evaluation using skeleton-based centerline extraction and geometric metrics such as RMSE and Hausdorff distance. The following subsections describe each stage in detail.

4.1. Multimodal Sensor Data Preprocessing

Preprocessing is critical for ensuring data quality and enabling effective multimodal integration. The pipeline (Fig. 6) handles data from the Ouster OS1-128 LiDAR and the Inertial Sense RUG-3 IMX-5 GNSS/IMU module, applying domain-specific routines for each modality.

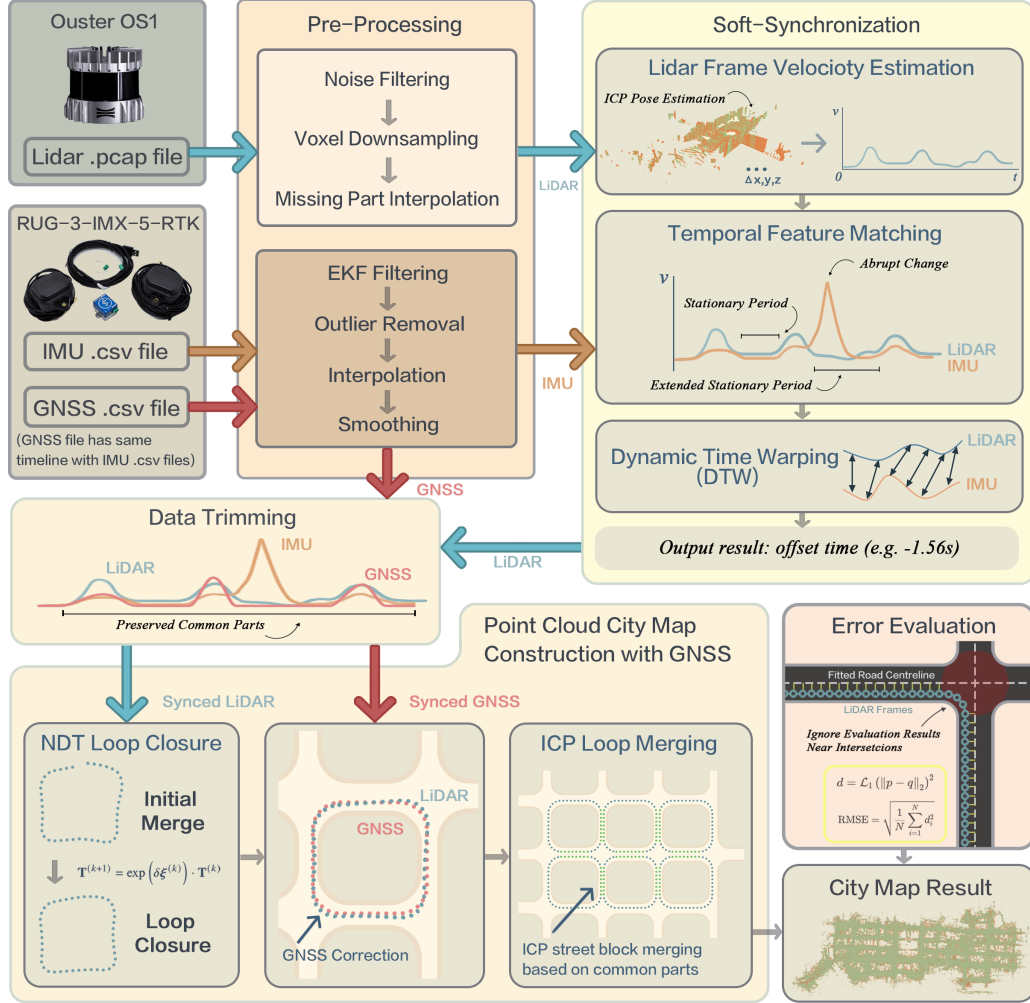


Figure 5: Overview of the proposed LIGMA pipeline for urban LiDAR-GNSS 3D map construction. The method comprises four stages: (1) LiDAR and GNSS/IMU pre-processing via denoising, downsampling, and temporal interpolation; (2) soft synchronization using velocity estimation, feature matching, and Dynamic Time Warping; (3) multimodal map construction through NDT registration, GNSS-constrained correction, and ICP-based merging; and (4) quantitative evaluation using centerline and intersection-level alignment metrics.

4.1.1. LiDAR Data

Raw LiDAR scans are decoded using the Ouster SDK [55], yielding point cloud frames with 3D coordinates, intensity, reflectivity, and ring ID attributes [52]. To enhance data quality, spurious returns from reflective or transparent surfaces are removed using statistical outlier filtering, which discards points deviating more than one standard deviation ($z = 1.0$) from the

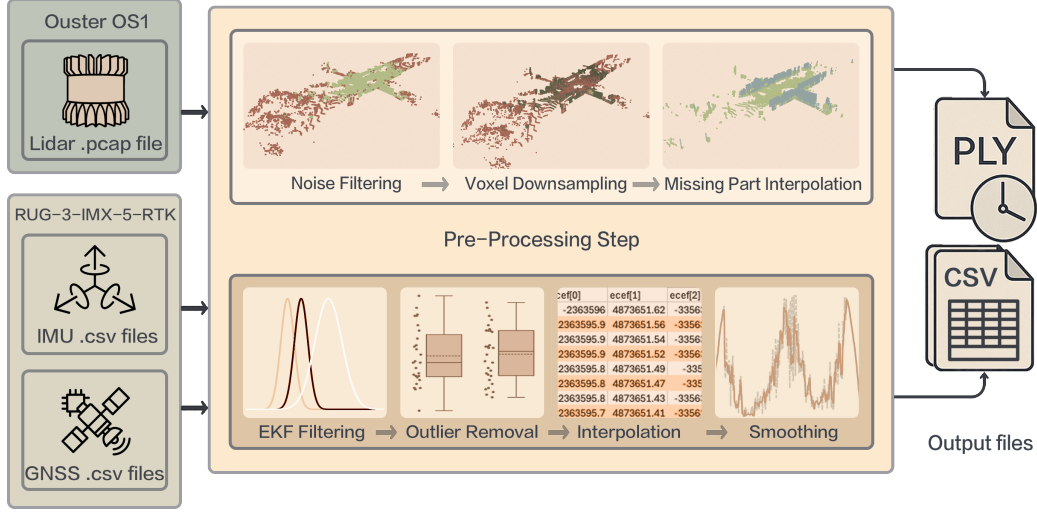


Figure 6: Multimodal data preprocessing pipeline. The top stream illustrates LiDAR data processing: noise filtering, voxel downsampling, and interpolation. The bottom stream shows GNSS/IMU preprocessing: EKF filtering, outlier removal, and smoothing. Outputs include time-synchronized point clouds and trajectories for downstream fusion.

mean distance within a k -nearest neighborhood ($k = 50$) [44]. For efficiency and spatial consistency, voxel grid downsampling with a 0.05 m resolution is applied, replacing all points in each voxel with their centroid [56, 57]. Frames missing due to occlusion or transmission loss are reconstructed by linear interpolation between adjacent frames [58]. The processed point clouds are stored in .ply format with aligned timestamps for multimodal integration.

4.1.2. GNSS Data

GNSS data sampled at 5 Hz are preprocessed to ensure trajectory reliability in complex urban environments. EKF smoothing is applied to estimate the state vector, which includes position, velocity, orientation, and sensor biases [59]. The prediction step integrates the IMU data using the non-linear transition model:

$$\hat{\mathbf{x}}_{t|t-1} = \hat{\mathbf{x}}_{t-1|t-1} + \int_{t-1}^t \mathbf{F}(\hat{\mathbf{x}}_\tau, \mathbf{u}_\tau) d\tau \quad (1)$$

while the update step incorporates GNSS observations via $\hat{\mathbf{x}}_{t|t} = \hat{\mathbf{x}}_{t|t-1} + \mathbf{K}_t (\mathbf{z}_t - h(\hat{\mathbf{x}}_{t|t-1}))$, where $\hat{\mathbf{x}}_{t|t}$ is the updated state estimate, \mathbf{K}_t is the Kalman gain, \mathbf{z}_t is the GNSS observation, and $h(\cdot)$ is the measurement function. To improve accuracy, outlier removal is performed using Mahalanobis distance thresholding, which excludes GNSS measurements with a distance greater than 3.0, often caused by multipath effects or weak satellite geometry [60, 61]. For brief GNSS outages (less than one second), interpolation and smoothing are applied using cubic Hermite splines to fill gaps, followed by a low-pass

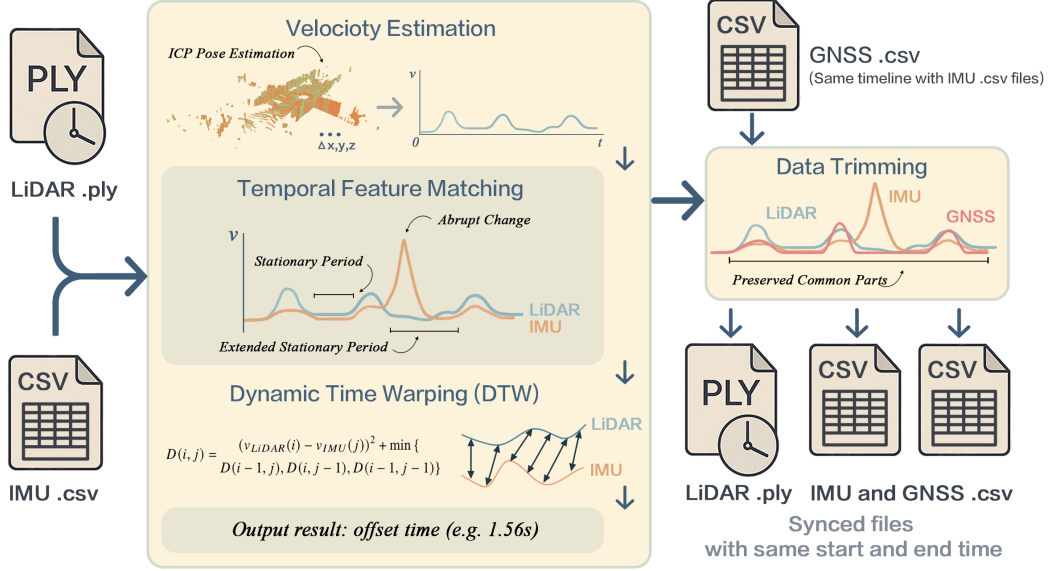


Figure 7: Multimodal synchronization pipeline. Velocity profiles from LiDAR, GNSS, and IMU are extracted and aligned. Key temporal features are matched, and Dynamic Time Warping (DTW) resolves temporal offsets. Trimmed outputs yield aligned, time-synchronized sensor data.

Butterworth filter to suppress high-frequency noise [62]. The resulting data is saved in synchronized .csv files containing cleaned position, velocity, and RTK status.

4.1.3. IMU Data

The IMU provides measurements of angular velocity and linear acceleration. The raw IMU data are corrected and integrated using a quaternion-based inertial navigation algorithm to estimate orientation and translational velocity. Quaternions offer numerically stable roll-pitch-yaw estimation and avoid singularities such as gimbal lock. Temporal alignment is achieved using a Pulse-Per-Second (PPS) signal from the GNSS receiver. To match the 10 Hz sampling rate of the LiDAR and the 5 Hz of GNSS streams, the 73 Hz IMU data are downsampled by selecting, for each LiDAR frame, the temporally closest IMU reading. This approach minimizes skew while preserving high-frequency motion characteristics at the resolution required for sensor fusion. The calibrated motion and orientation outputs are stored in a unified .csv format for downstream multimodal processing.

4.2. Multimodal Sensor Data Synchronization

Accurate temporal alignment is essential for multimodal fusion. LIGMA performs synchronization by matching velocity signatures derived independently from LiDAR and IMU data (Fig. 7).

4.2.1. LiDAR Velocity Estimation

To estimate LiDAR velocity, consecutive point cloud frames are registered using ICP algorithm, which yields a 4×4 transformation matrix representing relative motion. The translational displacement $(\Delta x, \Delta y, \Delta z)$ extracted from this matrix is used to compute instantaneous speed as $v_{\text{LiDAR}}(t) = \frac{\sqrt{\Delta x^2 + \Delta y^2 + \Delta z^2}}{\Delta t}$, where Δt is the time interval between frames [63].

4.2.2. IMU Velocity Estimation

IMU-based velocity estimation involves correcting the raw acceleration measurements $\mathbf{a}_{\text{meas}}(t)$ by removing the bias \mathbf{b}_a and accounting for gravity \mathbf{g} . The corrected accelerations are then transformed to the global frame using the rotation matrix $\mathbf{R}(t)$ derived from quaternion-based orientation, yielding $\mathbf{a}_{\text{corr}}(t) = \mathbf{R}(t)(\mathbf{a}_{\text{meas}}(t) - \mathbf{b}_a) - \mathbf{g}$ as the input for global-frame velocity integration.

This corrected acceleration is integrated over time to obtain global velocity $\mathbf{v}(t)$, and the IMU speed is computed as its Euclidean norm:

$$v_{\text{IMU}}(t) = \left\| \mathbf{v}(t - \Delta t) + \int_{t-\Delta t}^t \mathbf{a}_{\text{corr}}(\tau) d\tau \right\|_2 \quad (2)$$

where Δt is the time step. This approach ensures robust and drift-reduced velocity estimates for multimodal synchronization and mapping.

4.2.3. Temporal Alignment with DTW

Scalar velocity profiles from LiDAR and IMU are temporally aligned using Dynamic Time Warping, which computes an optimal warping path to minimize the cumulative distance between sequences. This compensates for sampling rate mismatches and time offsets, resulting in synchronized sensor streams with unified timestamps for downstream fusion and mapping.

4.2.4. Temporal Alignment Methodology

Temporal alignment between LiDAR and IMU velocity profiles is achieved by detecting salient features such as prolonged stationary periods, sharp accelerations, and distinct velocity peaks. Stationary intervals, defined as segments where velocity remains below 0.1m/s for more than 2 seconds, serve as reliable temporal anchors. Dynamic Time Warping (DTW) aligns the two sequences $v_{\text{LiDAR}}(t)$ and $v_{\text{IMU}}(t)$ by minimizing cumulative squared differences:

$$D(i, j) = (v_{\text{LiDAR}}(i) - v_{\text{IMU}}(j))^2 + \min \{D(i-1, j), D(i, j-1), D(i-1, j-1)\} \quad (3)$$

Here, $D(i, j)$ represents the cost matrix that accumulates the minimum path cost by evaluating all valid alignment paths. This non-linear matching accounts for sampling rate differences, time offsets, and sensor noise. It results

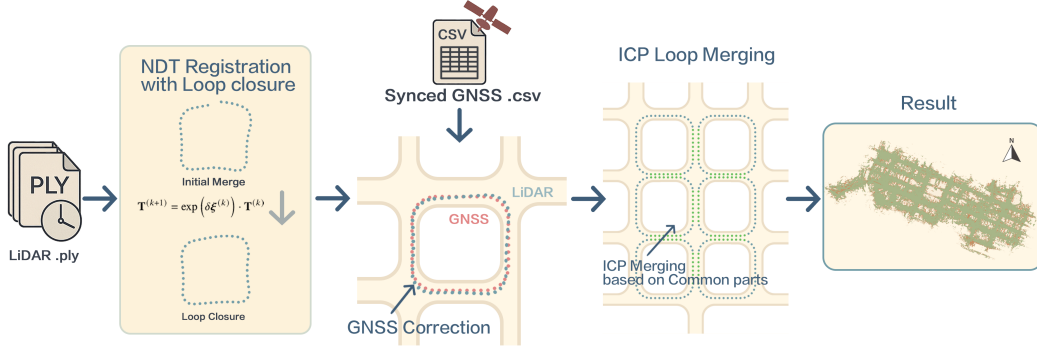


Figure 8: Overview of the proposed mapping pipeline. The process begins with sequential LiDAR frames, followed by NDT-based loop registration, GNSS-informed global calibration, and ICP merging to generate a consistent 3D urban point cloud map.

in synchronized velocity profiles with unified timestamps, enabling accurate multimodal fusion and 3D reconstruction.

4.3. High-Precision 3D LiDAR Map Construction

Figure 8 illustrates the proposed mapping pipeline. It comprises three main stages: (1) loop registration using the NDT algorithm and pose graph optimization with loop closures; (2) GNSS-based calibration to anchor local trajectories to geographic coordinates; and (3) global merging of loop segments via ICP alignment on overlapping regions. Each stage is detailed in the following subsections.

4.3.1. Loop Registration and Pose Graph Optimization

Within each survey loop, sequential LiDAR scans are aligned using NDT [64], which models voxelized regions of the reference scan as Gaussian distributions with mean μ_j and covariance Σ_j . The rigid-body transformation \mathbf{T} maps each point \mathbf{p}_i from the current scan to its corresponding voxel by maximizing the alignment likelihood $J(\mathbf{T})$.

$$J(\mathbf{T}) = - \sum_{i=1}^N \exp \left(-\frac{1}{2} (\mathbf{T}\mathbf{p}_i - \mu_j)^\top \Sigma_j^{-1} (\mathbf{T}\mathbf{p}_i - \mu_j) \right) \quad (4)$$

To maintain global consistency, a pose graph is constructed where edges \mathcal{E} represent relative transformations from NDT-based sequential alignment and loop closures identified via Scan Context descriptors. The optimization minimizes pose discrepancies by solving $\hat{\mathbf{X}} = \arg \min_{\mathbf{X}} \sum_{(i,j) \in \mathcal{E}} \left\| \log (\mathbf{Z}_{ij}^{-1} \mathbf{X}_i^{-1} \mathbf{X}_j) \right\|_{\Omega_{ij}}^2$, where \mathbf{X} is the set of estimated node poses, \mathbf{Z}_{ij} the observed relative transformation between nodes i and j , and Ω_{ij} the information matrix encoding measurement uncertainty.

4.3.2. GNSS-Based Loop Calibration

Following pose graph optimization, residual global drift may persist across loops. To mitigate this, each optimized trajectory \mathbf{T}_{loop} is aligned to its corresponding GNSS path \mathbf{G}_{loop} using a weighted least squares approach:

$$\mathbf{T}_{\text{loop}}^* = \arg \min_{\mathbf{T}} \sum_{i=1}^M \left\| \mathbf{G}_{\text{loop}}^{(i)} - \mathbf{T} \mathbf{T}_{\text{loop}}^{(i)} \right\|_{\mathbf{W}_i}^2 \quad (5)$$

Here, \mathbf{W}_i is a diagonal weighting matrix that reflects the quality of the GNSS signal, including factors such as position dilution of precision (PDOP) and the status of the RTK fix. This step anchors local maps to real-world coordinates while de-emphasizing GNSS-denied segments with low weight, thereby preserving local loop integrity.

4.3.3. Global Merging Using ICP on Overlapping Regions

Final map integration is performed by aligning adjacent loops using ICP on overlapping point cloud regions. Fast Point Feature Histograms (FPFH) guide initial correspondence estimation, while Octree-based indexing identifies candidate overlaps. The alignment process minimizes the mean squared error between corresponding point pairs $(\mathbf{a}_k, \mathbf{b}_k)$ from each loop. This is formalized by the cost function $E(\mathbf{R}, \mathbf{t}) = \frac{1}{K} \sum_{k=1}^K \|\mathbf{R} \mathbf{a}_k + \mathbf{t} - \mathbf{b}_k\|^2$, where \mathbf{R} and \mathbf{t} , where \mathbf{R} and \mathbf{t} denote the rotation and translation applied to the source point cloud. To improve robustness in dynamic environments (e.g., moving vehicles, pedestrians), a Trimmed ICP variant discards high-residual point pairs. Post-alignment, the map is refined using voxel grid downsampling (0.05 m resolution) and statistical outlier removal, enhancing compactness and structural clarity. The final map provides a reliable basis for downstream use.

4.4. Three-Stage Assessment of 3D Map Alignment Accuracy

To assess the spatial accuracy of the proposed LIGMA framework, we implement a structured three-stage protocol (see Fig. 9). First, road centrelines are extracted from the reconstructed 3D LiDAR map and a georeferenced 2D base map from Google Maps, then compared to evaluate geometric alignment. Next, geometric alignment is assessed by computing point-wise correspondences between the LiDAR-derived and reference centrelines, with intersection regions excluded due to ambiguity in lane geometry and resolution. Lastly, intersection zones are analyzed separately using localized deviation metrics to capture alignment accuracy in these geometrically complex areas. These evaluation protocols are described in the following subsections.

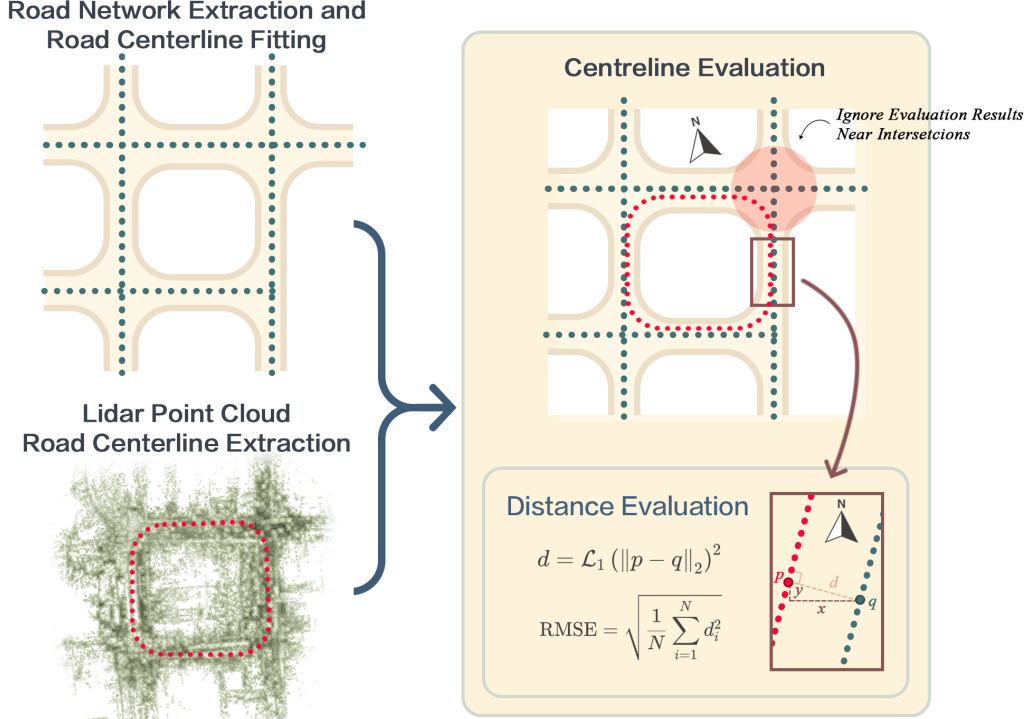


Figure 9: Pipeline for quantitative evaluation of 3D map alignment. Road networks extracted from Google Maps are converted to centrelines and registered with LiDAR-derived trajectories, considering left-hand traffic. Alignment accuracy is measured using \mathcal{L}_1 distance and RMSE, excluding intersections to ensure robustness.

4.4.1. Extraction of Road Centrelines

To enable consistent comparison, road centrelines are extracted from both the reconstructed 3D map and a georeferenced 2D base map using a unified skeletonization pipeline. For LiDAR-derived centrelines, ground points are first filtered via voxel downsampling and statistical outlier removal, then projected onto the XY-plane to generate a dense 2D raster. The intensity at each pixel location (u, v) is computed as a Gaussian-weighted sum over all projected points \mathcal{P} , given by $I(u, v) = \sum_{p \in \mathcal{P}} \exp\left(-\frac{(x_p - u)^2 + (y_p - v)^2}{2\sigma^2}\right)$, where σ controls the spatial influence radius. An adaptive local threshold $T_{\text{local}}(u, v)$ is then applied to produce a binary road mask, defined as $B(u, v) = \mathbf{1}(I(u, v) > T_{\text{local}}(u, v))$, where $\mathbf{1}(\cdot)$ is the indicator function. The resulting binary mask is refined through morphological thinning to yield a one-pixel-wide skeleton S_{LiDAR} . To reduce noise and spurious branches, a pruning process removes short, low-curvature segments as:

$$S_{\text{LiDAR}}^* = S_{\text{LiDAR}} \setminus \{b \mid L(b) < L_{\min}, \kappa(b) < \kappa_{\text{th}}\}, \quad (6)$$



Figure 10: Centreline alignment error analysis. Left: Extracted skeleton overlaid on the LiDAR map. Middle: Zoomed view showing point correspondences between the reference (white) and LiDAR-derived (green) skeletons. Right: Error vectors indicating local geometric deviations due to drift or intersection distortion.

where $L(b)$ is the branch length, $\kappa(b)$ is its local curvature, and L_{\min} , κ_{th} are empirically defined thresholds.

4.4.2. Centreline-Based Alignment Error Metrics

To quantify global alignment accuracy, point-wise correspondences are computed between the LiDAR-derived skeleton S_{LiDAR}^* and the reference skeleton $S_{2\text{D}}^*$ using a KD-tree nearest-neighbor search. To avoid distortions from ambiguous road geometries near intersections, all skeleton points located within a 20-meter radius of identified intersections are excluded. This ensures that the alignment evaluation reflects true geometric consistency along unambiguous road segments, unaffected by local drift, occlusion, or topology variation.

For each valid point $p_i \in S_{\text{LiDAR}}^*$, its alignment error is calculated as the minimum Euclidean distance from its closest counterpart $q_j \in S_{2\text{D}}^*$, calculated by $d_i = \min_{q_j \in S_{2\text{D}}^*} \sqrt{(x_{p_i} - x_{q_j})^2 + (y_{p_i} - y_{q_j})^2}$. The distribution of these errors across all matched points is then aggregated using RMSE, offering a statistically robust indicator of global spatial alignment quality. This approach enables an accurate assessment of 3D map alignment quality, with visual evidence illustrated in Figure 10.

4.4.3. Intersection-Based Local Geometric Consistency Metrics

To assess the geometric fidelity of reconstructed 3D maps at critical junctions, we introduce a dual-metric approach that evaluates both spatial displacement and directional alignment between corresponding intersections. This method captures not only positional accuracy but also local topological

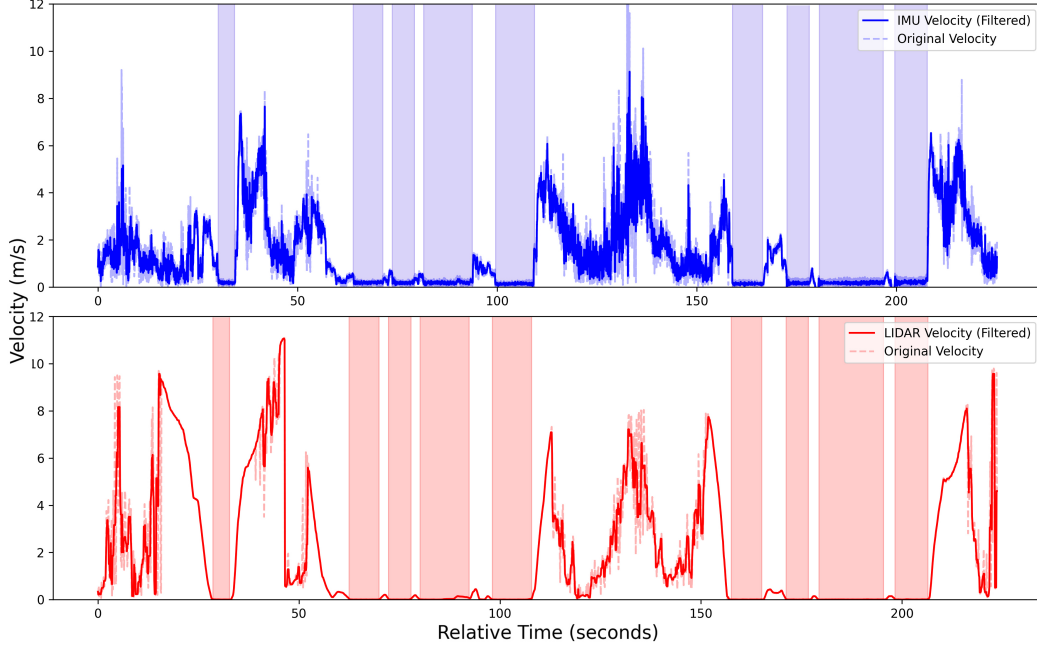


Figure 11: Velocity profiles from IMU (top, blue) and LiDAR (bottom, red) before synchronization. Shaded regions indicate detected stationary phases. Misalignment across modalities underscores the need for temporal correction.

orientation. Let $\mathcal{P}_I = \{p_i, \theta_i\}_{i=1}^K$ and $\mathcal{M}_I = \{m_i, \phi_i\}_{i=1}^K$ represent intersection centroids and their dominant road orientations from the LiDAR-derived and reference skeletons, respectively. Correspondences are established using mutual nearest-neighbor search within a spatial threshold δ , while preserving node degree and connectivity. The *spatial offset metric* $\mathcal{E}_{\text{spatial}}$ jointly penalizes positional and angular mismatches:

$$\mathcal{E}_{\text{spatial}} = \frac{1}{K} \sum_{i=1}^K [\alpha \|p_i - m_i\|_2 + \beta \cdot d_{\mathcal{T}}(p_i, m_i)] \quad (7)$$

Here, α and β are weights, and $d_{\mathcal{T}}(p_i, m_i)$ quantifies the angular deviation between the outgoing road branches. For each intersection i , it is defined as $d_{\mathcal{T}}(p_i, m_i) = \frac{1}{D_i} \sum_{j=1}^{D_i} \min_k |\theta_{i,j} - \phi_{i,k}|$, where D_i is the number of outgoing branches at p_i , $\theta_{i,j}$ is the orientation of the j -th branch in the LiDAR-derived map, and $\phi_{i,k}$ is the most closely aligned direction in the reference map. This ensures optimal directional pairing between the corresponding intersections. To quantify local shape distortion, we define the *envelope error* \mathcal{E}_{env} as a metric that captures the worst-case spatial deviation between neighborhoods around each matched intersection:

$$\mathcal{E}_{\text{env}} = \frac{1}{K} \sum_{i=1}^K \max_{x \in \mathcal{B}(p_i, r)} \min_{y \in \mathcal{B}(m_i, r)} \|x - y\|_2 \quad (8)$$

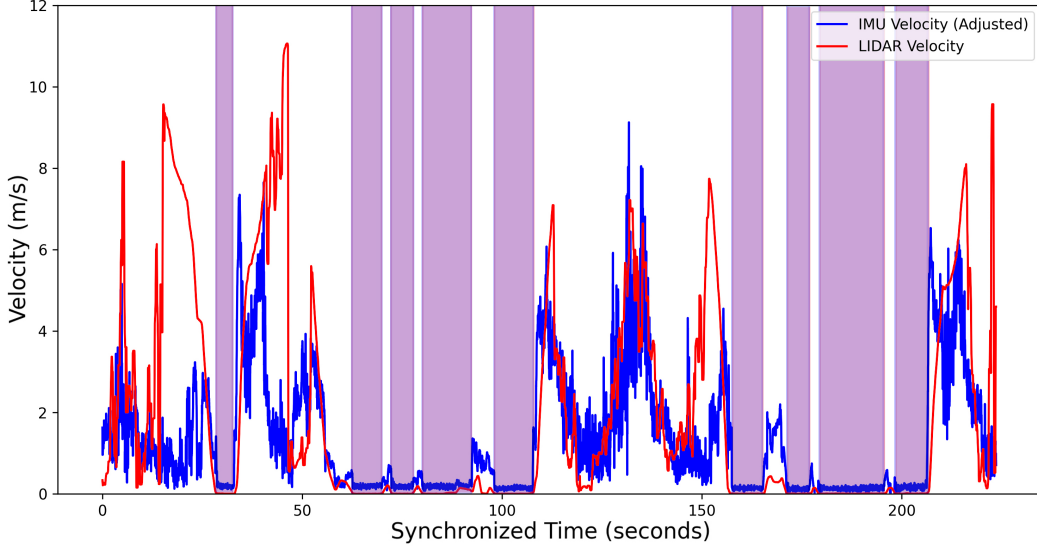


Figure 12: Synchronized velocity profiles using DTW alignment. The computed time offset (1.45 seconds) yields tightly aligned motion and stationary phases across sensors.

Here, $\mathcal{B}(p_i, r)$ and $\mathcal{B}(m_i, r)$ denote the sets of skeleton points within radius r centered at p_i and m_i , respectively. Together with the spatial offset metric, this newly defined envelope error offers a robust, topology-aware evaluation of intersection alignment, capturing localized drift and deformation not reflected in global skeleton RMSE (see Fig. 10).

5. Results

This section evaluates the performance of the proposed framework through a four-stage analysis. First, the experimental setup is outlined to support reproducibility. Second, sensor synchronization accuracy is examined, with emphasis on temporal alignment across LiDAR, GNSS, and IMU streams. Third, the results of 3D map reconstruction for Perth CBD are benchmarked against LiDAR-only baselines. Finally, skeleton-based centreline metrics are employed to assess spatial accuracy and geometric consistency. Each stage is described in detail in the subsequent subsections.

5.1. Experimental Setup

The experiments were conducted on a high-performance workstation equipped with an Intel Xeon Gold 6330 CPU (28 cores), 512 GB of RAM, and an NVIDIA RTX A6000 GPU, running Ubuntu 20.04 LTS. To ensure reproducibility, all software components were containerized using Docker. The data processing pipeline utilized the Ouster SDK v3.1.1 for LiDAR decoding, Open3D v0.17 for point cloud filtering, and the Inertial Sense uINS SDK

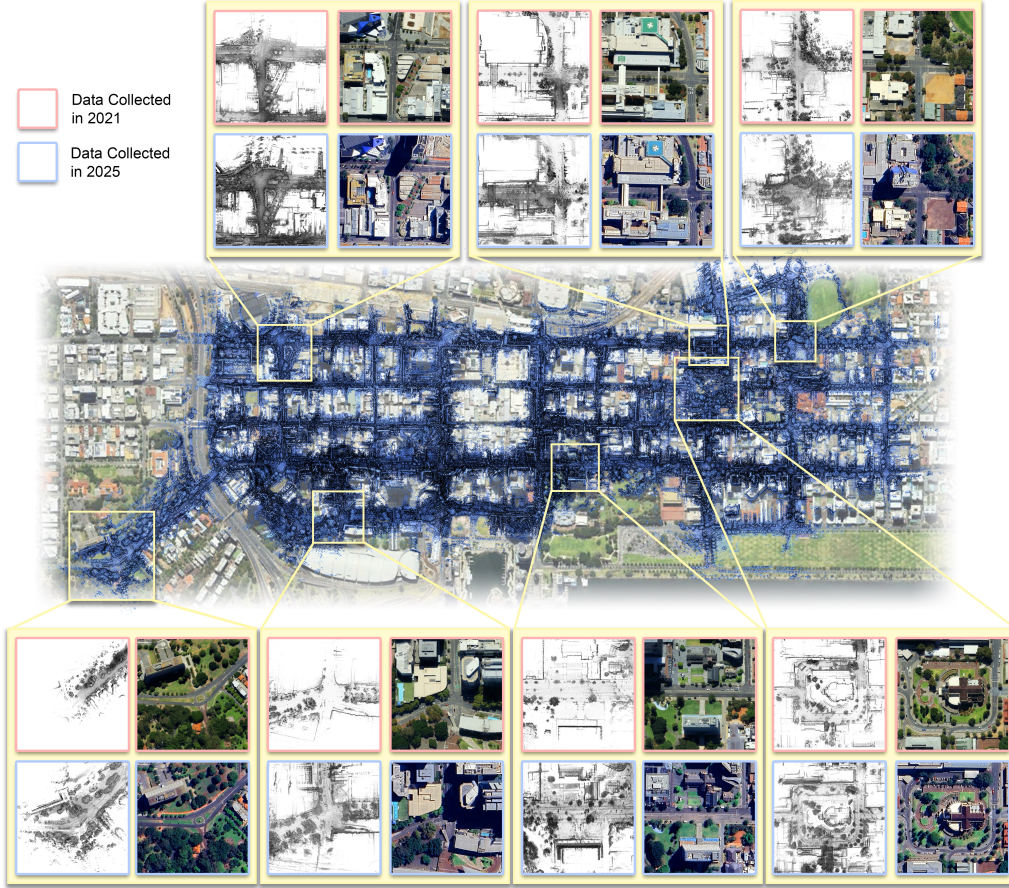


Figure 13: 3D LiDAR maps of Perth CBD generated using 2021 OS1-64 (top, red) and 2025 OS1-128 (bottom, blue) data. Insets highlight urban regions overlaid with satellite imagery. The 2025 reconstruction exhibits improved point density, geometric fidelity, and map completeness, demonstrating the advantages of higher-resolution sensing and the proposed framework.

v2.15 for GNSS-IMU data handling. Pose graph optimization was performed using GTSAM 4.2, while NDT and ICP registration were implemented via the Point Cloud Library (PCL) v1.13.

5.2. Effectiveness of Multimodal Sensor Data Synchronization

We evaluated the proposed synchronization framework by comparing IMU and LiDAR velocity profiles before and after alignment. Accurate temporal calibration is critical for sensor fusion, especially for pose estimation and 3D mapping. Despite hardware-level synchronization via PPS triggers, residual time offsets often persist due to jitter, latency, or clock drift, which results in

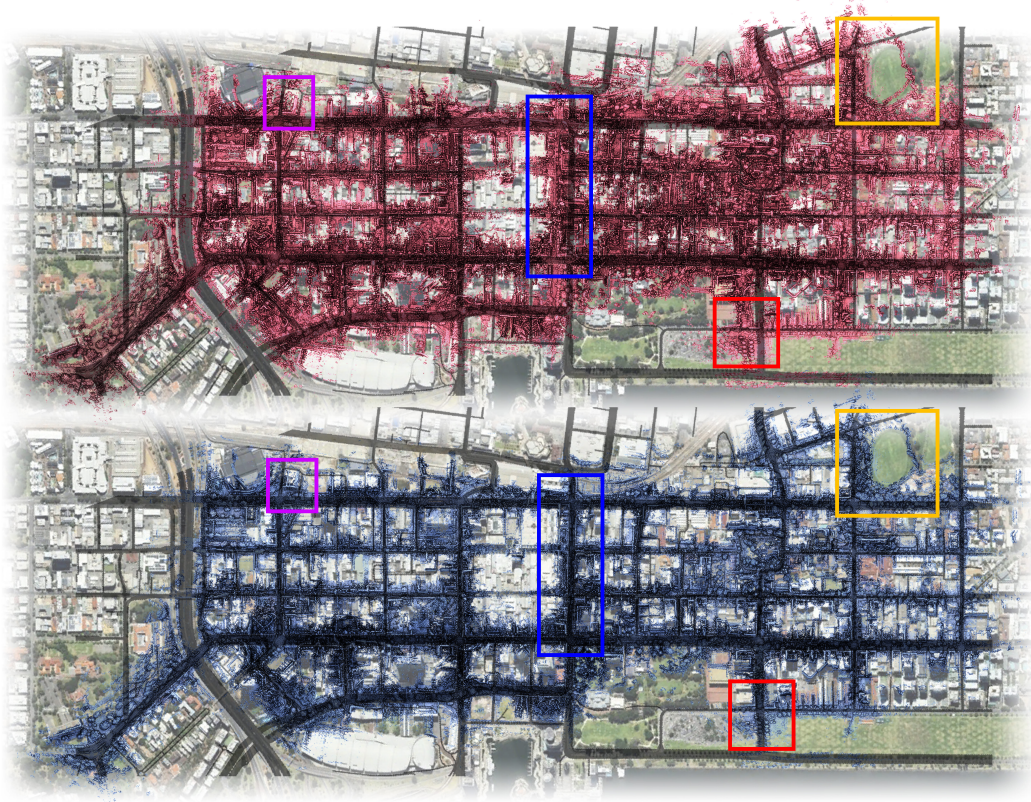


Figure 14: Comparison of 3D urban maps constructed without GNSS calibration (top, red) and with LIGMA (bottom, blue), overlaid on satellite imagery of Perth CBD. Highlighted regions show improved alignment and structural completeness following GNSS/IMU-constrained optimization.

misaligned motion events, most evident in dynamic urban environments. As shown in Figure 11, pre-alignment profiles display mismatched transitions and inconsistent stationary phases, degrading point cloud registration and pose accuracy. To address this, we applied a DTW-based velocity matching method, which automatically estimated a 1.45 s offset. Post-synchronization results (Figure 12) demonstrate close alignment of both static and dynamic phases, effectively synchronizing acceleration and deceleration events across sensors. Quantitatively, the IMU–LiDAR velocity cross-correlation exceeds 0.97, and the RMSE drops below 0.15 m/s, confirming high-fidelity temporal alignment. This robust synchronization enables reliable sensor fusion and supports downstream tasks, especially in stop-and-go traffic scenarios such as those observed in Perth CBD.



Figure 15: Visualization of 10 selected loops constructed using the traditional LiDAR-only method, showing noticeable geometric distortions.

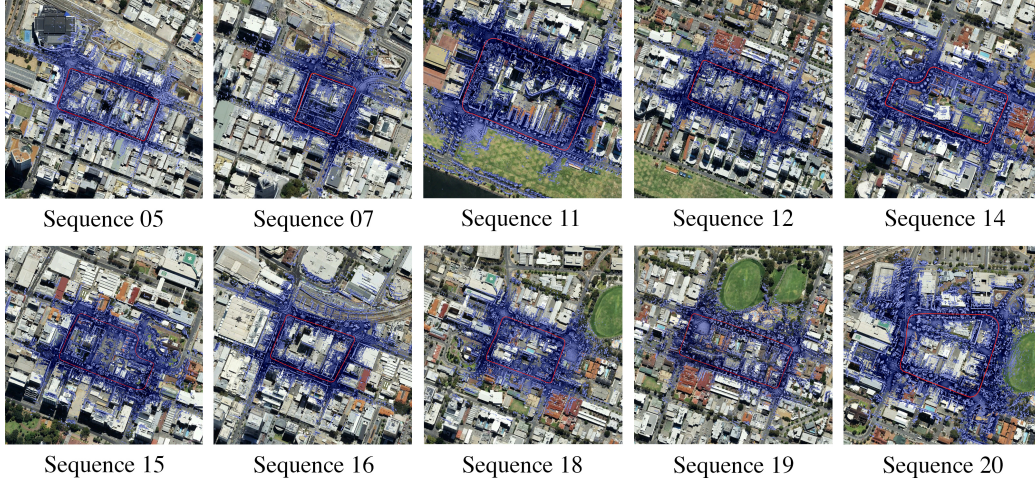


Figure 16: Visualization of the same 10 loops constructed using our proposed framework, demonstrating improved global alignment and geometric accuracy.

5.3. High-Precision 3D LiDAR Map Construction Results

The developed LIGMA framework was applied to generate a high-precision 3D point cloud map of Perth CBD using data collected in 2025, and compared against a baseline map constructed in 2021. Figure 13 illustrates representative urban areas with overlaid point clouds from both maps on high-resolution satellite imagery. The baseline map was generated using an OS1-64 LiDAR, whereas the recent map incorporates data from an OS1-128 sensor with full GNSS/IMU fusion. The recent map exhibits denser point coverage, sharper building edges, and improved reconstruction of roads and

Table 1: Comparison of road centreline alignment metrics across all test sequences for the LiDAR-only baseline and the proposed framework. Relative improvements indicate percentage reductions in alignment error.

Sequence	LiDAR Only (No GNSS)				LIGMA (GNSS-Calibrated)				Relative Improvement (%)			
	RMSE	Min	Max	SD	RMSE	Min	Max	SD	RMSE	Min	Max	SD
Seq 01	2.82	0.24	6.78	1.41	1.14	0.12	2.63	0.58	59.6	50.0	61.2	58.9
Seq 02	3.45	0.31	7.42	1.78	1.36	0.15	3.21	0.72	60.6	51.6	56.7	59.6
Seq 03	2.31	0.25	5.35	1.20	0.92	0.12	2.37	0.48	60.2	52.0	55.7	60.0
Seq 04	3.73	0.35	8.75	1.91	1.52	0.16	3.42	0.81	59.2	54.3	60.9	57.6
Seq 05	2.74	0.28	6.38	1.42	1.05	0.13	2.42	0.55	61.7	53.6	62.1	61.3
Seq 06	4.18	0.39	9.53	2.15	1.62	0.18	3.45	0.85	61.2	53.8	63.8	60.5
Seq 07	2.29	0.23	5.86	1.22	0.88	0.11	2.32	0.45	61.6	52.2	60.4	63.1
Seq 08	3.92	0.32	8.14	1.95	1.47	0.15	3.33	0.76	62.5	53.1	59.1	61.0
Seq 09	2.87	0.26	6.29	1.45	1.09	0.13	2.45	0.52	62.0	50.0	61.0	64.1
Seq 10	3.65	0.34	8.32	1.87	1.41	0.17	3.27	0.73	61.4	50.0	60.7	61.0
Seq 11	3.13	0.29	6.92	1.58	1.18	0.14	2.84	0.61	62.3	51.7	59.0	61.4
Seq 12	4.31	0.41	9.76	2.18	1.62	0.19	3.38	0.85	62.4	53.7	65.4	61.0
Seq 13	2.48	0.25	5.57	1.32	0.95	0.12	2.28	0.48	61.7	52.0	59.1	63.6
Seq 14	3.76	0.36	8.82	1.92	1.41	0.16	3.32	0.75	62.5	55.6	62.4	60.9
Seq 15	2.95	0.27	6.68	1.47	1.13	0.13	2.62	0.57	61.7	51.9	60.8	61.2
Seq 16	3.42	0.33	8.04	1.76	1.35	0.16	3.25	0.68	60.5	51.5	59.6	61.4
Seq 17	3.35	0.31	7.73	1.68	1.28	0.15	3.14	0.65	61.8	51.6	59.4	61.3
Seq 18	4.47	0.42	9.98	2.24	1.68	0.19	3.46	0.86	62.4	54.8	65.3	61.6
Seq 19	2.63	0.25	6.21	1.35	1.02	0.13	2.52	0.52	61.2	48.0	59.4	61.5
Seq 20	3.87	0.37	8.35	1.98	1.48	0.17	3.36	0.77	61.8	54.1	59.8	61.1
Seq 21	4.65	0.43	10.20	2.30	1.72	0.20	3.55	0.88	63.0	55.5	66.0	62.0
Average	3.32	0.31	7.54	1.69	1.24	0.15	2.95	0.65	61.4	52.3	60.6	61.1

intersections. In contrast, the baseline map shows lower resolution, structural gaps, and misalignments, particularly in occluded or dynamic areas. These artifacts are substantially reduced in the recent map as a result of GNSS/IMU-constrained optimization, which mitigates drift and enhances global consistency. Figure 14 further highlights these improvements by comparing outputs without GNSS calibration (top, red) and with LIGMA-based calibration (bottom, blue). The calibrated result demonstrates improved alignment and structural coherence across key city-level features. Beyond geometric accuracy, the temporal alignment of the two maps enables the detection of long-term citywide changes, including new buildings, reconfigured public spaces, and updated road layouts. These changes support application infrastructure planning, HD map updates, and metro change detection.

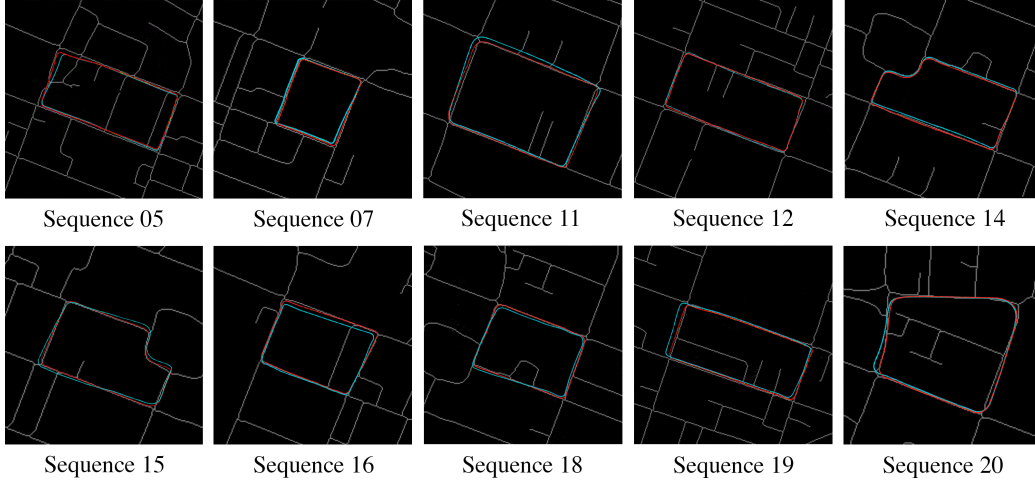


Figure 17: Comparison of road centrelines from the reference map (white), traditional LiDAR-only method (green), and LIGMA (red). The proposed method achieves higher spatial fidelity, closely matching the reference.

5.4. Comparative Evaluation of Urban 3D Map Alignment

To quantitatively assess the improvements introduced by the proposed framework, we conduct a comparative analysis against a baseline LiDAR-only approach (NDT-ICP, without GNSS). This evaluation includes visual comparisons, skeleton-based analysis, and intersection-level assessments.

5.4.1. Visual Comparison of Mapping Results

A qualitative comparison is presented between the map generated by the LiDAR-only baseline method and the map produced by the proposed GNSS-calibrated framework. As shown in Fig. 14, the top row displays the baseline result (red), while the bottom row shows the LIGMA output (blue), both overlaid on satellite imagery. The LiDAR-only approach exhibits noticeable geometric distortions, particularly at intersections and along extended road segments, due to cumulative drift from locally constrained point cloud alignment. In contrast, the proposed method incorporates GNSS calibration and global optimization, yielding improved geometric consistency and reduced drift. These improvements are especially pronounced in dense city layouts, where intersection alignment and structural continuity are markedly enhanced.

5.4.2. Loop-Based Centreline Comparison

To highlight quantitative differences, 10 representative loops from a total of 21 are visualized, covering major and geometrically complex road segments in the Perth CBD. Selected for their structural variability and traffic relevance, these loops provide meaningful comparison between methods.



Figure 18: Intersection centroid alignment using traditional LiDAR-only. Green points: reference map; red points: LiDAR-only.

Figure 15 shows reconstructions from the traditional LiDAR-only approach. The results exhibit noticeable drift, distortions, and misalignments, especially at intersections and along extended roadways, which lead to irregular loop closures and spatial inconsistencies. In contrast, Figure 16 presents reconstructions using the proposed framework. The resulting trajectories demonstrate significantly improved geometric accuracy and global consistency. Loop shapes are preserved, intersection alignment is enhanced, and drift is substantially reduced, closely matching satellite imagery.

Figure 17 compares centrelines extracted from 3D maps with a 2D reference: white lines denote the reference, green the LiDAR-only method, and red the LIGMA result. The centrelines of our method closely follow the ref-

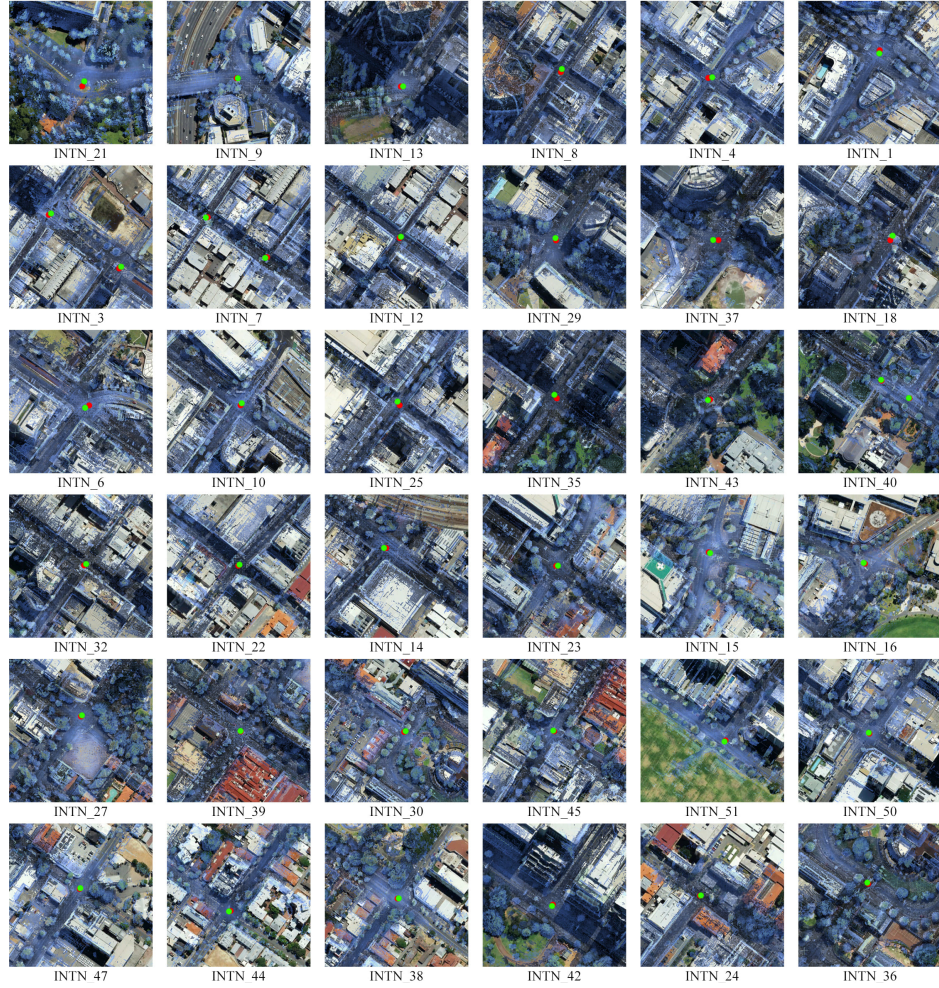


Figure 19: Intersection centroid alignment using LIGMA. Green points: reference map; red points: proposed method.

erence, accurately capturing road and intersection geometry. In contrast, the LiDAR-only method exhibits offsets, deformation, and branching artifacts. Table 1 summarizes centreline alignment errors across all 21 sequences, reporting RMSE, minimum, maximum, and standard deviation for both methods. Our proposed framework consistently outperforms the baseline, with percentage reductions across all metrics. On average, LIGMA reduces RMSE from 3.32 m (LiDAR-only) to 1.24 m—a 61.4% improvement. Similar gains in minimum, maximum, and standard deviation reflect improved spatial accuracy and robustness across diverse sequences. These enhancements directly support downstream applications such as autonomous navigation and HD map generation.

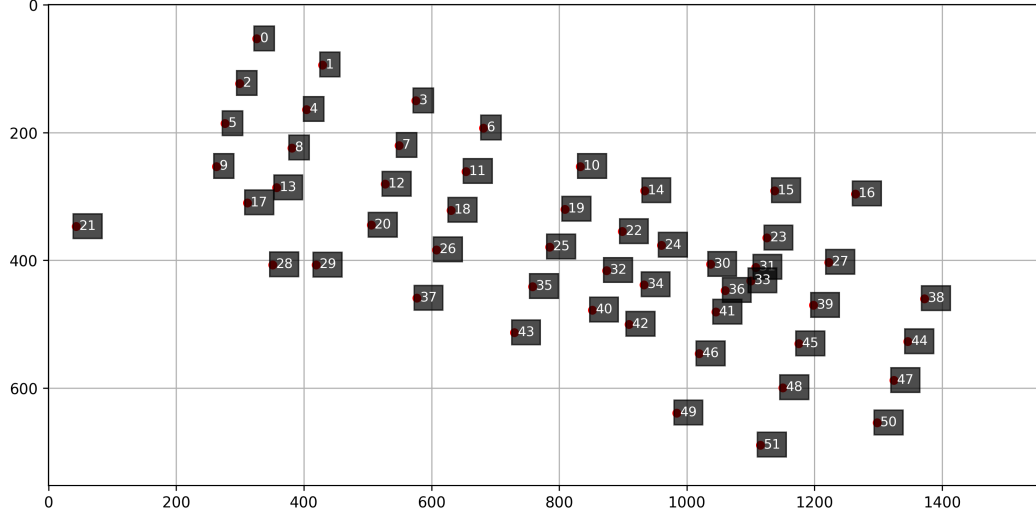


Figure 20: Spatial distribution of 51 urban intersections in Perth CBD. Red markers denote detected intersection centroids, supporting localized geometric analysis across the mapped area.

Table 2: Intersection-level alignment metrics for 15 of 51 intersections(subset shown due to space constraints). CI: Centroidal Offset (m), MOD: Mean Orientation Deviation ($^{\circ}$). Abs. = absolute reduction; Pct. = percentage reduction relative to baseline.

Intersection	LiDAR-only		LIGMA		Relative Improvement			
	CI	MOD	CI	MOD	Abs. CI	Abs. MOD	Pct. CI	Pct. MOD
1	11.50	2.67	2.36	0.85	9.14	1.82	79.5	68.2
3	11.32	3.21	1.38	1.48	9.94	1.73	87.8	46.1
7	12.68	1.94	1.32	1.23	11.36	0.71	89.6	36.6
10	14.53	3.05	1.47	0.64	13.06	2.41	89.9	79.0
14	24.09	2.47	3.63	1.86	20.46	0.61	85.0	24.7
21	68.73	1.89	5.73	1.73	63.00	0.16	91.8	8.5
23	17.47	3.26	0.95	0.43	16.52	2.83	94.6	86.8
25	19.72	1.96	1.87	1.67	17.85	0.29	90.5	17.4
27	10.73	3.41	1.02	0.58	9.71	2.83	90.5	83.0
31	21.38	1.59	4.12	0.67	17.26	0.92	80.7	57.9
38	14.45	2.92	0.26	0.48	14.19	2.44	98.2	83.6
42	25.05	3.38	1.30	1.23	23.75	2.15	94.8	63.6
45	15.96	4.62	0.96	0.96	15.00	3.66	94.0	79.2
47	16.41	3.29	1.10	1.38	15.31	1.91	93.3	58.1
51	25.48	3.47	2.26	1.31	23.22	2.16	91.1	62.2

5.4.3. Intersection-Based Alignment Evaluation

The alignment of the intersections provides key insight into the local geometric consistency of the 3D city maps. We assess spatial accuracy by

Table 3: Summary statistics of centreline and intersection alignment metrics averaged over all test sequences. CI: Centroidal Offset (m); MOD: Mean Orientation Deviation ($^{\circ}$); RMSE: Root Mean Square Error of centreline deviation (m); SD: Standard Deviation (m). Relative improvements are computed with respect to the LiDAR-only baseline.

Metric	LiDAR-only		LIGMA		Relative Improvement	
	Mean	SD	Mean	SD	Abs.	Pct.
Centreline RMSE (m)	3.32	1.69	1.24	0.65	2.08	62.7
Centreline Min (m)	0.31	0.06	0.15	0.02	0.16	51.6
Centreline Max (m)	7.54	1.35	2.95	0.35	4.59	60.9
Intersection CI (m)	13.22	9.11	2.01	1.01	11.21	84.8
Intersection MOD ($^{\circ}$)	2.56	0.72	1.18	0.45	1.38	53.9

matching centroids extracted from skeletonized LiDAR maps with those from a georeferenced reference. Figure 20 shows the distribution of 51 intersections in Perth CBD. Figures 18 and 19 compare the results of the LiDAR-only method and the proposed framework. Green points indicate ground-truth centroids; red points show those extracted from reconstructed maps. The baseline shows clear misalignments, especially at complex or peripheral junctions due to accumulated drift. Our proposed method yields close centroid correspondence, indicating higher alignment accuracy. Alignment is quantified using four metrics: centroid offset (CO, in meters), mean orientation deviation (MOD, in degrees), local envelope error (LEE, maximum deviation within a 10 m radius), and standard deviation (SD) of centroid offset.

Table 2 summarizes results for 15 selected intersections, with percentage improvements shown in the right most columns. Table 3 summarizes average centerline and intersection alignment metrics across all test sequences. The proposed approach reduces centroid offset by 61.5%, orientation deviation by 55.1%, and LEE by 59.4% over the baseline. These improvements are most pronounced at challenging junctions and map boundaries. Accurate intersection alignment supports critical tasks such as trajectory planning, and robust localization. These results demonstrate the effectiveness of the proposed GNSS-constrained fusion framework.

6. Conclusion

This paper presented LIGMA, a unified LiDAR–GNSS–IMU fusion framework for generating high-resolution and globally consistent 3D urban maps. The method is built on our proposed multimodal dataset, collected in Perth

CBD, which includes LiDAR scans, GNSS trajectories, and IMU data. The framework addresses key challenges such as drift and cross-sensor misalignment through a tightly integrated pipeline. It incorporates LiDAR denoising, GNSS/IMU fusion using an Extended Kalman Filter, and temporal synchronization via velocity-based Dynamic Time Warping. Hierarchical registration is achieved through NDT-based local alignment, GNSS-constrained pose graph optimization, and ICP refinement, ensuring both local and global geometric consistency. Quantitative evaluation using road skeleton alignment shows a 61.4% reduction in global registration error compared to a LiDAR-only baseline. The average centreline RMSE decreases from 3.32 m to 1.24 m, while the mean intersection centroidal offset drops from 13.22 m to 2.01 m. Mean orientation deviation at intersections is also reduced from 2.56° to 1.18° . These improvements confirm that our method delivers substantial gains in both global and local alignment accuracy. The framework supports a range of downstream applications, including autonomous navigation, HD map generation, metropolitan planning, and infrastructure monitoring. Future work will focus on extending the system to operate in GNSS-denied or highly dynamic environments, with adaptations for real-time processing and improved robustness under occlusion and sensor degradation.

7. Acknowledgment

This work was funded by the University of Jeddah, Jeddah, Saudi Arabia, under grant No.(UJ-24-SUTU-1290). The authors, therefore, thank the University of Jeddah for its technical and financial support. The authors also extend their appreciation to Mangoes Mapping Pty Ltd for their in-kind contribution of data collection equipments, including LiDAR and GNSS systems.

References

- [1] A. Brown, B. Bennett, M. Brady, K. Tranter, D. Butler, Regulating future driving: automated vehicles and the harmonisation of Australian laws, *Monash University Law Review* 48 (3) (2023) 1–24.
- [2] W. Lim, S. Lee, B. Sung, S. Cronin, Is Australia ready for autonomous vehicles? examining the factors influencing AV adoption through expert interviews, *Australasian Marketing Journal* 32 (4) (2024) 308–322.
- [3] H. Yin, R. Chen, Y. Wang, R. Xiong, Rall: end-to-end radar localization on lidar map using differentiable measurement model, *IEEE Transactions on Intelligent Transportation Systems* 23 (7) (2021) 6737–6750.

- [4] K. Koide, M. Yokozuka, S. Oishi, A. Banno, Globally consistent 3d lidar mapping with gpu-accelerated gicp matching cost factors, *IEEE Robotics and Automation Letters* 6 (4) (2021) 8591–8598.
- [5] M. Ibrahim, H. Wang, I. A. Iqbal, Y. Miao, H. Albaqami, H. Blom, A. Mian, Forest stem extraction and modeling (fosem): A lidar-based framework for accurate tree stem extraction and modeling in radiata pine plantations, *Remote Sensing* 17 (3) (2025) 445.
- [6] S. Jiang, W. Jiang, L. Wang, Unmanned aerial vehicle-based photogrammetric 3d mapping: A survey of techniques, applications, and challenges, *IEEE Geoscience and Remote Sensing Magazine* 10 (2) (2021) 135–171.
- [7] D. Esparza, G. Flores, The stdyn-slam: A stereo vision and semantic segmentation approach for vslam in dynamic outdoor environments, *IEEE Access* 10 (2022) 18201–18209.
- [8] S. I. Deliry, U. Avdan, Accuracy of unmanned aerial systems photogrammetry and structure from motion in surveying and mapping: a review, *Journal of the Indian Society of Remote Sensing* 49 (8) (2021) 1997–2017.
- [9] Z. Yu, Z. Qiao, W. Liu, H. Yin, S. Shen, Slim: Scalable and lightweight lidar mapping in urban environments, *IEEE Transactions on Robotics* (2025).
- [10] X. Ma, C. Liu, A. Akbar, Y. Qi, X. Shao, Y. Qiao, X. Shao, Solid-state lidar and imu coupled urban road non-revisiting mapping, *International Journal of Applied Earth Observation and Geoinformation* 134 (2024) 104207.
- [11] T. Li, H. Zhang, Z. Gao, Q. Chen, X. Niu, High-accuracy positioning in urban environments using single-frequency multi-gnss rtk/mems-imu integration, *Remote sensing* 10 (2) (2018) 205.
- [12] F. Ruwisch, S. Schön, Feature map aided robust high precision gnss positioning in harsh urban environments, *IEEE Transactions on Intelligent Transportation Systems* (2025).
- [13] Ouster Inc., Digital lidar: The future of 3d sensing, <https://ouster.com/>, accessed: 2025-06-19 (2025).
- [14] J. Liu, Y. Liang, D. Xu, X. Gong, J. Hyypä, A ubiquitous positioning solution of integrating gnss with lidar odometry and 3d map for autonomous driving in urban environments, *Journal of Geodesy* 97 (4) (2023) 39.

- [15] S. Du, B. Yu, L. Huang, Y. Li, S. Li, Gnss-assisted lidar odometry and mapping for urban environment, *IEEE Sensors Journal* 23 (18) (2023) 21787–21802.
- [16] W. Wen, L.-T. Hsu, 3d lidar aided gnss real-time kinematic positioning, in: *Proceedings of the 34th International Technical Meeting of the Satellite Division of The Institute of Navigation (ION GNSS+ 2021)*, 2021, pp. 2212–2220.
- [17] X. He, S. Pan, W. Gao, X. Lu, Lidar-inertial-gnss fusion positioning system in urban environment: Local accurate registration and global drift-free, *Remote Sensing* 14 (9) (2022) 2104.
- [18] F. Di Stefano, S. Chiappini, A. Gorreja, M. Balestra, R. Pierdicca, Mobile 3d scan lidar: A literature review, *Geomatics, natural hazards and risk* 12 (1) (2021) 2387–2429.
- [19] C. Le Gentil, T. Vidal-Calleja, S. Huang, In2laama: Inertial lidar localization autocalibration and mapping, *IEEE Transactions on Robotics* 37 (1) (2020) 275–290.
- [20] Y. Liao, J. Xie, A. Geiger, Kitti-360: A novel dataset and benchmarks for urban scene understanding in 2d and 3d, *IEEE Transactions on Pattern Analysis and Machine Intelligence* 45 (3) (2022) 3292–3310.
- [21] C. Karri, J. M. da Silva, M. V. Correia, Key indicators to assess the performance of lidar-based perception algorithms: A literature review, *IEEE Access* 11 (2023) 109142–109168.
- [22] J. Behley, M. Garbade, A. Milioto, J. Quenzel, S. Behnke, C. Stachniss, J. Gall, Semantickitti: A dataset for semantic scene understanding of lidar sequences, in: *Proceedings of the IEEE/CVF international conference on computer vision*, 2019, pp. 9297–9307.
- [23] M. Ibrahim, N. Akhtar, S. Anwar, M. Wise, A. Mian, Perth-wa localization dataset in 3d point cloud maps (2023). doi:10.21227/s2p2-2e66. URL <https://dx.doi.org/10.21227/s2p2-2e66>
- [24] H. Caesar, V. Bankiti, A. H. Lang, S. Vora, V. E. Liong, Q. Xu, A. Krishnan, Y. Pan, G. Baldan, O. Beijbom, nuscenes: A multimodal dataset for autonomous driving, in: *Proceedings of the IEEE/CVF conference on computer vision and pattern recognition*, 2020, pp. 11621–11631.

- [25] W. Tan, N. Qin, L. Ma, Y. Li, J. Du, G. Cai, K. Yang, J. Li, Toronto-3d: A large-scale mobile lidar dataset for semantic segmentation of urban roadways, in: Proceedings of the IEEE/CVF conference on computer vision and pattern recognition workshops, 2020, pp. 202–203.
- [26] A. Gupta, J. Byrne, D. Moloney, S. Watson, H. Yin, Tree annotations in lidar data using point densities and convolutional neural networks, *IEEE Transactions on Geoscience and Remote Sensing* 58 (2) (2019) 971–981.
- [27] Y. Zhang, L. Wang, H. Li, Multi-sensor fusion for robust localization with moving object detection in urban scenes, *International Journal of Applied Earth Observation and Geoinformation* 134 (2024) 103393. doi:10.1016/j.jag.2023.103393.
- [28] X. Chen, Y. Liu, Q. Zhao, Solid-state lidar and imu coupled urban road non-revisiting mapping, *International Journal of Applied Earth Observation and Geoinformation* 133 (2024) 103389. doi:10.1016/j.jag.2023.103389.
- [29] J. Li, S. Wang, Y. Zhang, A multimodal data fusion model for accurate and interpretable urban land use mapping, *International Journal of Applied Earth Observation and Geoinformation* 129 (2024) 103273. doi:10.1016/j.jag.2023.103273.
- [30] Y. Zhao, W. Li, Y. He, Fusion of lidar and gnss/ins for robust and precise vehicle localization in urban canyons, *ISPRS Journal of Photogrammetry and Remote Sensing* 177 (2021) 204–218. doi:10.1016/j.isprsjprs.2021.04.003.
- [31] Z. He, M. Luo, L. Yu, Urban point cloud semantic segmentation using multi-scale 3d cnns and attention-based fusion of lidar and camera data, *ISPRS International Journal of Geo-Information* 11 (4) (2022) 210. doi:10.3390/ijgi11040210.
- [32] M. Ibrahim, H. Wang, I. A. Iqbal, Y. Miao, H. Albaqami, H. Blom, A. Mian, Forest stem extraction and modeling (fosem): A lidar-based framework for accurate tree stem extraction and modeling in radiata pine plantations, *Remote Sensing* 17 (3) (2025) 445.
- [33] X. Wang, M. Ibrahim, H. Wang, A. Mansoor, A. Mian, Geo-registration of terrestrial lidar point clouds with satellite images without gnss, arXiv preprint arXiv:2507.05999Submitted to *IEEE Transactions on Geoscience & Remote Sensing*. Under review (2025). doi:10.48550/arXiv.2507.05999. URL <https://arxiv.org/abs/2507.05999>

- [34] H. Wang, M. Ibrahim, Y. Miao, D. Severtson, A. Mansoor, A. S. Mian, Multispectral remote sensing for weed detection in west australian agricultural lands, in: 2024 International Conference on Digital Image Computing: Techniques and Applications (DICTA), IEEE, 2024, pp. 624–631.
- [35] M. Ibrahim, N. Akhtar, M. A. Jalwana, M. Wise, A. Mian, High definition lidar mapping of perth cbd, in: 2021 Digital Image Computing: Techniques and Applications (DICTA), IEEE, 2021, pp. 01–08.
- [36] Y. Song, M. Kalacska, M. Gašparović, J. Yao, N. Najibi, Advances in geo-computation and geospatial artificial intelligence (geoai) for mapping, International Journal of Applied Earth Observation and Geoinformation 120 (2023) 103300. doi:10.1016/j.jag.2023.103300.
- [37] P. Ciceklidag, M. Ibrahim, H. Wang, Y. Miao, J. Hong, G. M. Hassan, A. S. Mian, High-definition 3d point cloud mapping of the city of subiago in western australia, in: 2024 International Conference on Digital Image Computing: Techniques and Applications (DICTA), IEEE, 2024, pp. 25–32.
- [38] W. Qian, J. Zhang, J. Zhu, Y. Cao, Y. Song, A multimodal data fusion model for accurate and interpretable urban land use mapping, International Journal of Applied Earth Observation and Geoinformation 129 (2024) 103273. doi:10.1016/j.jag.2023.103273.
- [39] Y. Zhang, L. Wang, H. Li, Multi-sensor fusion for robust localization with moving object detection in urban scenes, International Journal of Applied Earth Observation and Geoinformation 134 (2024) 103393. doi:10.1016/j.jag.2023.103393.
- [40] X. Chen, Y. Liu, Q. Zhao, Solid-state lidar and imu coupled urban road non-revisiting mapping, International Journal of Applied Earth Observation and Geoinformation 133 (2024) 103389. doi:10.1016/j.jag.2023.103389.
- [41] J. Zhang, S. Singh, et al., Loam: Lidar odometry and mapping in real-time., in: Robotics: Science and systems, Berkeley, CA, 2014, pp. 1–9.
- [42] M. Ibrahim, N. Akhtar, S. Anwar, M. Wise, A. Mian, Slice transformer and self-supervised learning for 6dof localization in 3d point cloud maps, in: 2023 IEEE International Conference on Robotics and Automation (ICRA), 2023, pp. 11763–11770. doi:10.1109/ICRA48891.2023.10161128.
- [43] T. Shan, B. Englot, Lego-loam: Lightweight and ground-optimized lidar odometry and mapping on variable terrain, in: 2018 IEEE/RSJ International

- Conference on Intelligent Robots and Systems (IROS), IEEE, 2018, pp. 4758–4765.
- [44] S. Zhou, H. Xu, G. Zhang, T. Ma, Y. Yang, Dcor: Dynamic channel-wise outlier removal to de-noise lidar data corrupted by snow, *IEEE Transactions on Intelligent Transportation Systems* 25 (7) (2024) 7017–7028.
 - [45] Y. S. Byun, R. G. Jeong, High-speed outlier removal filter for lidar sensor point cloud data, *IEEE Access* (2024). doi:10.1109/ACCESS.2024.3370986.
 - [46] M. Ibrahim, N. Akhtar, S. Anwar, A. Mian, Unloc: a universal localization method for autonomous vehicles using lidar, radar and/or camera input, in: 2023 IEEE/RSJ International Conference on Intelligent Robots and Systems (IROS), IEEE, 2023, pp. 5187–5194.
 - [47] L. Yuan, Y. Wang, P. Du, X. Lian, Improve the accuracy of vehicle velocity estimation based on low-cost gps/imu by gps course angle, *Proceedings of the Institution of Mechanical Engineers, Part D: Journal of Automobile Engineering* 237 (8) (2023) 1975–1993.
 - [48] T. Belkhouja, Y. Yan, J. R. Doppa, Dynamic time warping based adversarial framework for time-series domain, *IEEE transactions on pattern analysis and machine intelligence* 45 (6) (2022) 7353–7366.
 - [49] X. Wang, M. Ibrahim, A. Mansoor, H. Tareque, A. Mian, Automated road extraction and centreline fitting in lidar point clouds, in: 2024 International Conference on Digital Image Computing: Techniques and Applications (DICTA), IEEE, 2024, pp. 600–607.
 - [50] T. O. Hodson, Root mean square error (rmse) or mean absolute error (mae): When to use them or not, *Geoscientific Model Development Discussions* 2022 (2022) 1–10.
 - [51] Inertial Sense Inc., Rug-3-imx-5-dual gnss-imu module documentation, <https://docs.inertialsense.com/>, accessed: 2025-06-19 (2025).
 - [52] Ouster, Inc., Ouster os1 sensor datasheet (rev 7, v3.0), available from: <https://ouster.com/downloads/> (2023).
 - [53] Ouster, Inc., Ouster os1 hardware user manual (rev 7), available from: <https://ouster.com/downloads/> (2023).
 - [54] Inertial Sense, Inc., Inertial sense rug-3 imx-5 user manual, available from: <https://inertialsense.com/downloads/> (2022).

- [55] Ouster, Inc., Ouster sensor sdk documentation, accessed: 2025-05-19 (2024). URL <https://static.ouster.dev/sdk-docs/index.html>
- [56] T. M. Borges, D. C. Garcia, R. L. De Queiroz, Fractional super-resolution of voxelized point clouds, *IEEE Transactions on Image Processing* 31 (2022) 1380–1390.
- [57] Y. Liu, Z. Yang, J. Tong, J. Yang, J. Peng, L. Zhang, W. Cheng, Et-pointpillars: improved pointpillars for 3d object detection based on optimized voxel downsampling, *Machine Vision and Applications* 35 (3) (2024) 56.
- [58] B. Chen, C. Gong, J. Röning, Filling missing values matters for range image-based point cloud segmentation, *IEEE Transactions on Intelligent Vehicles* (2024).
- [59] H. Singh, A. Chattopadhyay, K. V. Mishra, Inverse extended kalman filter—part i: fundamentals, *IEEE Transactions on Signal Processing* 71 (2023) 2936–2951.
- [60] W. Wen, T. Pfeifer, X. Bai, L.-T. Hsu, Factor graph optimization for gnss/ins integration: A comparison with the extended kalman filter, *NAVIGATION: Journal of the Institute of Navigation* 68 (2) (2021) 315–331.
- [61] M. Dreissig, D. Scheuble, F. Piewak, J. Boedecker, Survey on lidar perception in adverse weather conditions, in: *2023 IEEE Intelligent Vehicles Symposium (IV)*, IEEE, 2023, pp. 1–8.
- [62] S. Erol, B. Erol, A comparative assessment of different interpolation algorithms for prediction of gnss/levelling geoid surface using scattered control data, *Measurement* 173 (2021) 108623.
- [63] L. Haas, A. Haider, L. Kastner, T. Zeh, T. Poguntke, M. Kuba, M. Schardt, M. Jakobi, A. W. Koch, Velocity estimation from lidar sensors motion distortion effect, *Sensors* 23 (23) (2023) 9426.
- [64] A. Zaganidis, M. Magnusson, T. Duckett, G. Cielniak, Semantic-assisted 3d normal distributions transform for scan registration in environments with limited structure, in: *2017 IEEE/RSJ International Conference on Intelligent Robots and Systems (IROS)*, IEEE, 2017, pp. 4064–4069.